Engineering Science and Technology, an International Journal 36 (2022) 101154

HOSTED BY

Contents lists available at ScienceDirect

Engineering Science and Technology, an International Journal

journal homepage: www.elsevier.com/locate/jestch

BTS-GAN: Computer-aided segmentation system for breast tumor using MRI and conditional adversarial networks

Imran Ul Haq [a], Haider Ali [a], Hong Yu Wang [b], Lei Cui [a], Jun Feng [a,*]

[a] School of Information Science and Technology, Northwest University, Xian, China
[b] School of computer Science, Xian University of Posts and Telecommunications, Xian, China

ARTICLE INFO

Article history:
Received 27 September 2021
Revised 9 March 2022
Accepted 11 April 2022

Keywords:
Generative adversarial networks
Breast MRI
Breast tumor
Parallel dilated convolution
Medical Image Segmentation

ABSTRACT

Breast tumor is one of the most prominent indicators for the diagnosis of breast cancer. The precise segmentation of tumors is crucial for enhancing the accuracy of breast cancer detection. A physician's assessment of the MRI scan is time-consuming and require a lot of human effort and expertise. Furthermore, traditional medical segmentation approaches frequently need prior information or manual feature extraction, resulting in a subjective diagnosis. Therefore, the development of an automated image segmentation approach is essential for clinical applications. This work presents BTS-GAN, an automatic breast tumor segmentation process using conditional GAN (cGAN) in Magnetic Resonance Imaging (MRI) scans. First, we used an encoder-decoder deep network with skip connections between encoder and decoder for the generator to increase the localization efficiency. Second, we utilized a parallel dilated convolution (PDC) module to retain the features of various sizes of masses and to effectively extract information about the masses' edges and interior texture. Third, an extra classification-related constraint is included to the loss function of the cGAN for mitigating the hard-to-converge challenge in image-to-image (I2I) translation tasks based on classification. The generator side of our proposed model learns to detect the tumor and construct a binary mask, while the discriminator learns to distinguish between ground truth and synthetic masks, driving the generator to produce masks as genuine as possible. The experimental results demonstrate that our BTS-GAN is more efficient and reliable for breast tumor segmentation and outperform other segmentation techniques in terms of the IoU and Dice coefficient on the publicly available RIDER breast cancer MRI dataset. Our proposed model achieved an average IoU and Dice scores of 77% and 85% respectively.

1. Introduction

Breast cancer is the most prevalent cancer in females at the moment and is one leading cause of women's mortality worldwide [1]. In 2018, about 627,000 fatalities due to breast cancer were recorded globally by the World Health Organization (2019), represents almost 15% of total fatalities from cancer in females. In addition, the prevalence of the breast cancer grows per year [2]. Fortunately, as stated by Liu, Tang, et al., the mortality of breast cancer is declining because of people's awareness about the disease and developments in medical technologies that enable its early identification and diagnoses [3]. To prevent the disease from further progression, adequate and on-time care will improve the chances of survival. According to the literature, there are almost 40% chances of survival on early detection [4]. However, in medical image analysis, one basic challenge is the correct segmentation to identify the boundaries of organs or lesions in images. The segmentation of image data is a critical step in the analysis of shapes, volume detection, and treatment arrangement for radiation therapy. Since manually annotating object boundaries is subjective and may be time-consuming, a reliable and accurate automatic segmentation technique is the requirement of clinical and research applications.

Mammography (MG) and Ultrasonography (US) are commonly utilized modalities for examining breast lesions due to their affordable price and exploitation facility. Yet, these approaches sometimes lack essential details needed to recognize the tumor under investigation. Moreover, US requires high analysis expertise due to low image quality [5], while MG is not a good choice due to high-density mammary glands. Magnetic Resonance Imaging (MRI) is an effective method in screening breast tumors recently.

* Corresponding authors.
E-mail addresses: imhaq123@yahoo.com (I.U. Haq), alihaider@stumail.nwu.edu.cn (H. Ali), hywang@xput.edu.cn (H.Y. Wang), leicui@nwu.edu.cn (L. Cui), fengjun@nwu.edu.cn (J. Feng).

https://doi.org/10.1016/j.jestch.2022.101154
2215-0986/

MRI generates multi-view visual representation and high quality images of the inspected body parts, particularly for soft tissues of the breast than both MG and US. In addition, MRI supports a number of sub-sequences like Dynamic Contrast Enhanced MRI (DCE-MRI). In the DCE-MRI exam, a paramagnetic contrast agent is inserted into the body, which causes images with relatively high intensity in the tumor region [6].The DCE-MRI permits a highly precise breast tumor follow-up. Militello et al. [7] proposed a semi-automated strategy for segmenting masses on DCE-MRI of the breast, using Fuzzy spatial clustering and got better results than other classical techniques.

Before the advancement of Deep Learning (DL), traditional Medical Image (MI) segmentation methods primarily comprise of level set based methods [8], watershed algorithms [9], region growing [10], Markov Random Fields [11], active contour models [12], and their extensions. However, these approaches only provide satisfactory results if the background and object area differ widely. Local feature limitations and curvature constraints are often added to models to increase the segmentation accuracy. However, when the object and background areas are identical, such solutions are still not effective. As a result, utilizing a DL algorithm to tackle medical image segmentation is a promising field of study with theoretical and practical implications.

The evolution of DL in medical image domain has a significant positive influence on disease diagnosis tools in medical image applications. Several research projects have been suggested for tasks such as medical image classification [13,14], detection [15] and segmentation [16–18]. In the near past, Convolutional Neural Networks (CNN) have accomplished great outcomes in segmentation tasks of medical images. Piantadosi et al. [19] used an ensemble of deep CNNs trained on 3D MR data to correctly segment breast parenchyma from the surrounding air and other tissues like the chest wall. In addition to using the latest techniques in the field, they used a multi-planar combination of U-Net CNNs utilizing a suitable projection-fusing strategy, which allows for multi-protocol applications. The proposed approach has been validated using two different datasets containing a total of 109 DCE-MRI studies with histopathologically confirmed lesions and two acquisition protocols. Wang et al. [20] proposed a 2D/3D mixed convolution module capable of exploiting contexts between adjacent slices in 90 DCE-MRI studies. A multi-scale context extractor block was presented to retrieve multi-scale image features, which are essential for breast lesions' shape and size diversity. Yousefikamal et al.[21] proposed an effective NN for Breast Tumor Segmentation (BTS) using mammogram scans. The author used a fuzzy approach by combining tumor region segmentation and classification. CNN was utilized for classification of images into normal, abnormal categories, while abnormal images were further segmented for tumors. Almajalid et al. [22] proposed a neural network for ultrasound images originally designed for microscopy image segmentation. The proposed model showed good results.

After CNN the Fully Convolutional Networks (FCN)[23] and U-Net [24] models are frequently employed nowadays for medical image segmentation. Moeskops et al.[25] proposed a Fully Connected Neural Network (FCNN) using MRI scans for breast pectoral muscle segmentation. The dataset contains a total of 34 MR scans. Antari et al. [26] proposed a three-stage automated CAD scheme for BTS using digital mammograms. The author adopted a YOLO network for tumor localization and a Full resolution Convolutional Network (FrCN) to isolate the ROIs. Lastly, classification was done using CNN. U-Net [24] is premised on the idea of FCN. It is composed of a feature extractor encoder and an image reformation decoder. Several enhancements and changes in U-Net to further enhance performance have recently been examined. Tong et al. [27] used a U-Net to segment the lung nodule. To speed up the training and minimize overfitting, U-Net was equipped with a batch normalization [28] layer. In order to locate the nipples area from the remaining breast area, Zhuang et al. [29] proposed a customized U-NET architecture to segment the nipples from full breast US images. For accurate segmentation of malignancy in breast US images, Zhuang et al.[30] developed another U-Net based model called RADU-Net. For breast segmentation, U-NET++ has been proposed by Jiao, H et al. using high contrast MRI scans [31]. Dalmis et al. [32] employed a U-Net based segmentation method for breast fibroglandular tissue (FGT) segmentation. While the U-Net technique for BT segmentation is effective, the features retrieved using U-Net are insufficient to identify the fine margins of the tumor and, in some instances, result in excessively segmented results, as illustrated in Fig. 7.

Employing Generative Adversarial Networks (GAN) [33] is another way to improve medical image segmentation and get more specific results. This is still a hot research subject at the moment. GANs significantly increases the quality of medical image segmentation by its excellent synthesizing capacity and potential to extract and distribute data. This technique has been found to increase semantic segmentation performance with the additional use of adversarial loss during training the model [34,35]. The generative network learns to detect the tumor and produce a binary mask, while the adversarial network learns to differentiate between actual and synthetic masks, compelling the generator to build realistic binary masks. Even with a small number of training data, the cGAN performs well. The use of adversarial loss as an extra global segmentation evaluation is anticipated to be a useful supplementary signal for segmentation models in general, and particularly for datasets of limited size [36] which are prevalent in cancer imaging datasets. Unlike traditional generative models, GAN does not require complicated probability calculations. The distribution type does not need to be specified, and deep neural networks directly mimic the distribution using real data. GANs have been widely utilized to create fictitious data for a variety of purposes, including image synthesis and dataset generation. GAN-based solutions are used effectively in the area of medical imaging [18,37–41]. Most recently, conditional Generative Adversarial Networks (cGAN) have been utilized for BTS and shape classification in mammogram scans. The results obtained using cGAN outperform other techniques of BT segmentation [42].

Inspired by the above performance of the GAN, we present a new U-Net based breast tumor segmentation GAN (BTS-GAN) system to segment the BT region in whole breast MRI scans. The generator of the proposed system is composed of an improved version of the U-Net, with a parallel dilated convolution (PDC) module between encoder and decoder. PDC has the ability to expand the receptive field, which allows it to capture breast masses of varying sizes and shapes without increasing the trainable parameters. The PDC block can help reduce the issue of small tumor-relevant characteristics being lost due to successive downsampling layers. The capabilities of the baseline U-Net were enhanced employing skip-connections and PDC. The enhanced U-Net was trained against a patch DCNN, used as the discriminator of our proposed BTS-GAN to further increase the performance. Moreover, we proposed a modified objective function by adding a classification related constraint to the objective of cGAN because BT segmentation is more like a pixel-level classification task than a regression task. The segmentation result became more stable and precise when the upgraded U-Net was trained versus the discriminator with a novel objective function. Contributions of the research are: (1) This research is the first to use the cGAN architecture with DCE-MRI images for breast tumor segmentation, (2) The PDC module is used to leverage image multi-scale and contextual information by constantly extending the receptive field at varying dilation rates without lowering the feature map resolution, (3) we added classification related constraints to the loss function for efficient

regularization of the cGAN to make it more efficient at solving the semantic segmentation (SS) task for medical images, (4) our segmentation method achieved better performance than U-Net and improved U-Net on the public dataset.

2. Motivation and methodology

2.1. Background

In 2014, Goodfellow et al. [33] presented GAN as a solution for modeling image data, which was subsequently utilized to create additional images. GAN contains two key modules, a Generator (G) and a Discriminator (D). These two modules are trained enough to solve the min–max game theory problem. The objective of the GAN is given by:

$$\min_G \max_D L(G,D) = \mathbb{E}_{u\sim P_{\text{data}}(u)}[\log D(u)] + \mathbb{E}_{w\sim P_w(z)}[\log(1 - D(G(w)))] \quad (1)$$

D is the discriminator and G represents generator, u represent real image, w is the arbitrary input to the generator, drawn from Pw, a probability distribution, G(w) is the output of G. D(G(w)), D(u) are the probabilities of the generated and real images respectively, judged by D.

The goal of GAN is to figure out how training data is distributed [17]. First of all, noise is introduced into generator G to achieve this goal. This noise is turned into an image by the G. During training, the G attempts to minimalize the objective function and fool D by generating similar images like the original, while the discriminator learns and tries to assign a high score to the real image and thus learn to discriminate between actual and generated input by maximizing the objective function. The cGAN is a GAN modification that enables us to control the generated image, for example, enabling us to generate an image of a specific class. As a result, cGANs are well-suited for I2I transformation tasks, in which an input image is conditioned and created an output. The objective of the cGAN has the following form to guarantee that the output image matches the input image.

$$\mathscr{L}_{cGAN}(G,D) = \mathbb{E}_{u,v}[\log D(u,v)] + \mathbb{E}_{u,w}[\log(1 - D(u,G(u,w)))] \quad (2)$$

Where in Eq. (2), v is the target image and $\mathscr{L}_{\text{cGAN}}$ is called the adversarial loss. The random variable z in dropout layers helps in producing deterministic results, avoiding overfitting. The adversarial loss is insufficient because of the model collapse problem, which can affect target domain output. The generator fools not only the discriminator but also output results that should be nearly similar to the ground truth. There is numerous information shared between input and output of the G for the image translation process; therefore, additional constraints are included to the objective loss function to guarantee the similarity among input and output of the generator. Therefore, L1 distance loss was added to the final objective to make sure the large similarity among input and output images of G. Mathematically, L1 is given as:

$$\mathscr{L}_{L1}(G) = \mathbb{E}_{u,v,w}[\|v - G(u,w)\|_1] \quad (3)$$

Eq. (3) is the generator L1 loss term. The above two loss functions were combined by Isola et al. [43] in their famous Pix2Pix algorithm for I2I translation task, which got super success in the domain. The Pix2Pix's loss function is calculated as:

$$L_{pix2pix} = \mathscr{L}_{cGAN}(G,D) + \lambda L_{L1}(G) \quad (4)$$

In Eq.(4), $\mathscr{L}_{\text{cGAN}}$ is the conditional loss and $\mathscr{L}_{\text{L1}}$ represents L1 distance between the fake and real masks. L1 regularizes G to produce images that are acceptable copies of the source image while $\mathscr{L}_{\text{cGAN}}$ determines whether the G can produce credible images in the target domain. $\mathscr{L}_{\text{pix2pix}}$ has successfully estimated the mapping functions for a wide range of I2I translation tasks [44–46]. However, when it came to SS of breast lesions, we discovered that it could not obtain a comparably accurate outcome. We think the reason behind is, their GAN loss technique treats I2I translation as regression problem, whereas SS is inherently a pixel-level dense classification task. As a result, we revised the issue by including the classification-related loss component, i.e., *cross entropy (CE)* loss, in the design of our GAN loss.

2.2. Proposed Model

Our proposed BTS-GAN is a supervised learning approach based on cGAN that needs data in pairs of input and target images. Suppose "A" is our source image, and "B" is our ground truth (binary mask) in the segmentation problem. The BTS-GAN's generator tries to generate a binary mask that should be similar to the B. Conversely, the discriminator network of the BTS-GAN learns whether the generated mask is same as the B, i.e., real or fake. The generator has a single image, both as its input and output, while the discriminator receives the generated output from the generator and its pair ground truth as input and tries to score the value. The score for the generator is calculated as an adversarial score which provides the potential to learn and output correct segmentation (binary mask). These two networks compete with each other in a min–max two player game theory. A simple overview of our proposed method for BT segmentation in MRI is shown in Fig. 1.

2.2.1. Loss function

The loss function of the BTS-GAN has the following form,

$$\mathscr{L}_{BTS-GAN}(G,D) = \mathscr{L}_{CGAN}(G,D) + \lambda[L_{L1}(G) + \mathscr{L}_{CE}(G)] \quad (5)$$

where $\mathscr{L}_{cGAN}(G,D)$ and $\mathscr{L}_{L1}(G)$ have the same definition as in Eq.(4), and L_{CE}(G) is the CE loss associated with the SS task. Since SS is a pixel-by-pixel classification problem, instead of a regression task, the $\mathscr{L}_{CE}(G)$ regularization term must enable our BTS-GAN to structure this I2I transformation task nearer to a classification problem. As a result, during adversarial training against D, our G having extra term $\mathscr{L}_{CE}$ would favor to develop satisfactory segmentation results. Generally, our final loss can be calculated as:

$$\text{Loss}_{\text{final}} = \arg\min_G \max_D \mathscr{L}_{CGAN}(G,D) + \lambda[\mathscr{L}_{L1}(G) + \mathscr{L}_{CE}(G)] \quad (6)$$

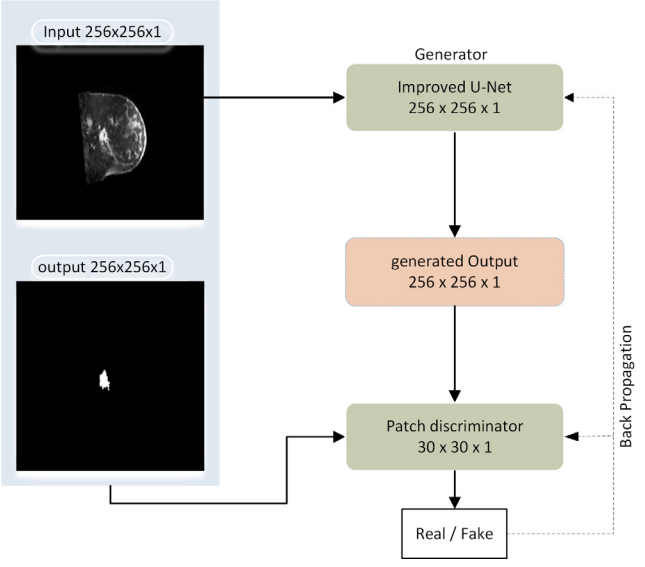

Fig. 1. A simple flow diagram of the proposed methodology for BTS.

In Eq. (6), one additional hyper-parameter lambda (λ) weighting is the generator means absolute error factor. The λ factor adjusts the adversarial and global losses [47].

2.2.2. Parallel dilated convolution module

In order to expand the receptive field of the convolution kernel without adding extra parameters in the SS task, the resolution of the feature map must be contracted by pooling or stride convolution [48,49]. Fig. 2 illustrates demonstrative diagrams of dilated convolution, which avoids the requirement to reduce the feature map's resolution by inserting "holes" into the convolution kernel to expand the receptive field and capture multi-scale semantic information in images. Three parallel convolution branches make up the PDC module. In particular, several dilated convolutions with different dilation rates are cascaded in a branch of the PDC module, which improves the representativeness of the feature maps for various scale targets. The output of each branch is then added element by element to achieve multi-scale feature fusion. Fig. 3 illustrates the PDC module in detail. In the first branch, feature sampling is implemented using a simple 3 x 3 convolution. Two and three 3 x 3 convolution operations are cascaded in the second and third branches, respectively. In the second branch, a basic 3 x 3 convolution and a dilated convolution with a rate of 2 are cascaded sequentially. The three 3 x 3 convolutional layers in the final branch have atrous rates of 1, 2, and 3, respectively. As a result, the PDC module preserves multi-scale and context information in the image while minimizing information loss in the surrounding pixels caused by a single dilated convolution.

2.2.3. Generator

For the generator, we used the U-NET [24] model architecture with custom modification. Mapping a high-resolution input grid to a high-resolution output grid is a defining aspect of I2I translation problems. Furthermore, the input and output for the problem we consider are both representations of a similar basic structure. As a result, the input structure is closely associated with the output structure. In a general encoder-decoder network, the input undergoes a series of down sampling levels till it reaches a bottleneck layer, at which point the process reverses. Here the information must pass through all levels, including the bottleneck. Many image translation problems share numerous low-level information between input and output, and it is preferable to transfer this data via the network directly. Skip-connections were inserted between layers of the same size of encoder-decoder to provide the G with a way of circumventing the bottleneck associated with this kind of data [24]. We also introduced a PDC [48] module between the encoder and decoder. Indeed, the PDC block aids the generator network in recognizing breast tumor-related characteristics at various scales and expanding the filters' real receptive field. As a result, the network becomes more sensitive to context without increasing the number of parameters or the cost of execution. The G and D architectures are shown in Fig. 4.

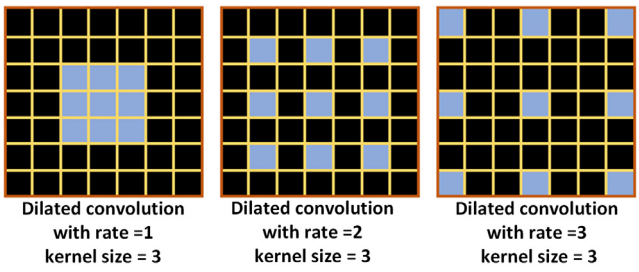

Fig. 2. Illustrative diagrams of dilated convolution with different atrous rates.

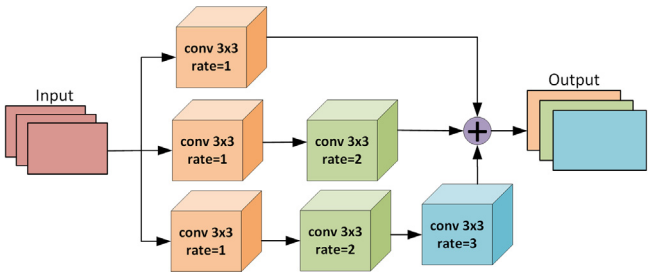

Fig. 3. Architecture of the PDC module.

Initially, the encoder is fed with an input breast MRI scan of 256 x 256 x 1 in dimension. The encoder has a total of seven convolution layers with a filter size of 4 x 4 followed by stride filters of size 2 for feature down sampling, a Leaky-ReLu with alpha equal to 0.2, followed by 2-dimensional batch normalization (BN), except in the first layer (conv1). BN substantially increases the generated segmentation samples' efficiency, stability, and excellence. The decoder block is the opposite of the encoder and transforms the latent variable into a volume of size 256 x 256 with one channel. After each upsampling layer, the features of the corresponding encoder layer are concatenated and thus expand the features map for the next decoder layer. The decoder has seven deconvolution layers with the same 4 x 4 filter size followed by a stride of 2 and ReLu with an alpha of 0.2. To avoid overfitting, a dropout of 0.02 was applied only in the first 3 up-sampling layers. All layers of convolution and deconvolution have been initialized using a zero-mean random initializer with a standard deviation value of 0.02. Convolution is used after the final level in the decoder, followed by a sigmoid function to map the output.

2.2.4. Patch-GAN Discriminator

The Discriminator of BTS-GAN is a Patch-GAN as used by Isola et al. [43] to classify images. This deep CNN classifies N $\times$ N patches of an input image as fake or real rather than the full image. We convolutionally applied this discriminator throughout the image and averaged all responses to obtain the final output of the discriminator. This is beneficial since a smaller Patch-GAN has small number of parameters, runs quicker, and has the ability to process images of any size. This type of discriminator takes the input as a *Markov random field*, with the assumption that pixels distanced by greater than a patch diameter are independent. Because discriminator training is closely linked to adversarial loss efficiency, BN is introduced to regularize and accelerate the training procedure.

The Patch-GAN discriminator's input tensor is a tensor constructed by concatenating the input-target pair and the input–output pair generated by G to provide an estimate of how genuine they appear. The network contains four 2-dimensional convolution layers, as in Fig. 4. Each of the convolution layers is convoluted with a filter size of 4$\times$4 with stride of 2. Each upsampling layer of the model undergoes BN and Leaky-ReLU. The output is further convoluted to make a probability patch of 30 $\times$ 30. Each value in the probability patch corresponded to a patch of the input images. In the last layer, the sigmoid activation function is used to produce the probability score of the input image being genuine (1) or fake (0).

3. Experiments and Results

3.1. Dataset

The RIDER (Reference Image Database to Evaluate therapy Response) breast MRI dataset was utilized to assess the perfor-

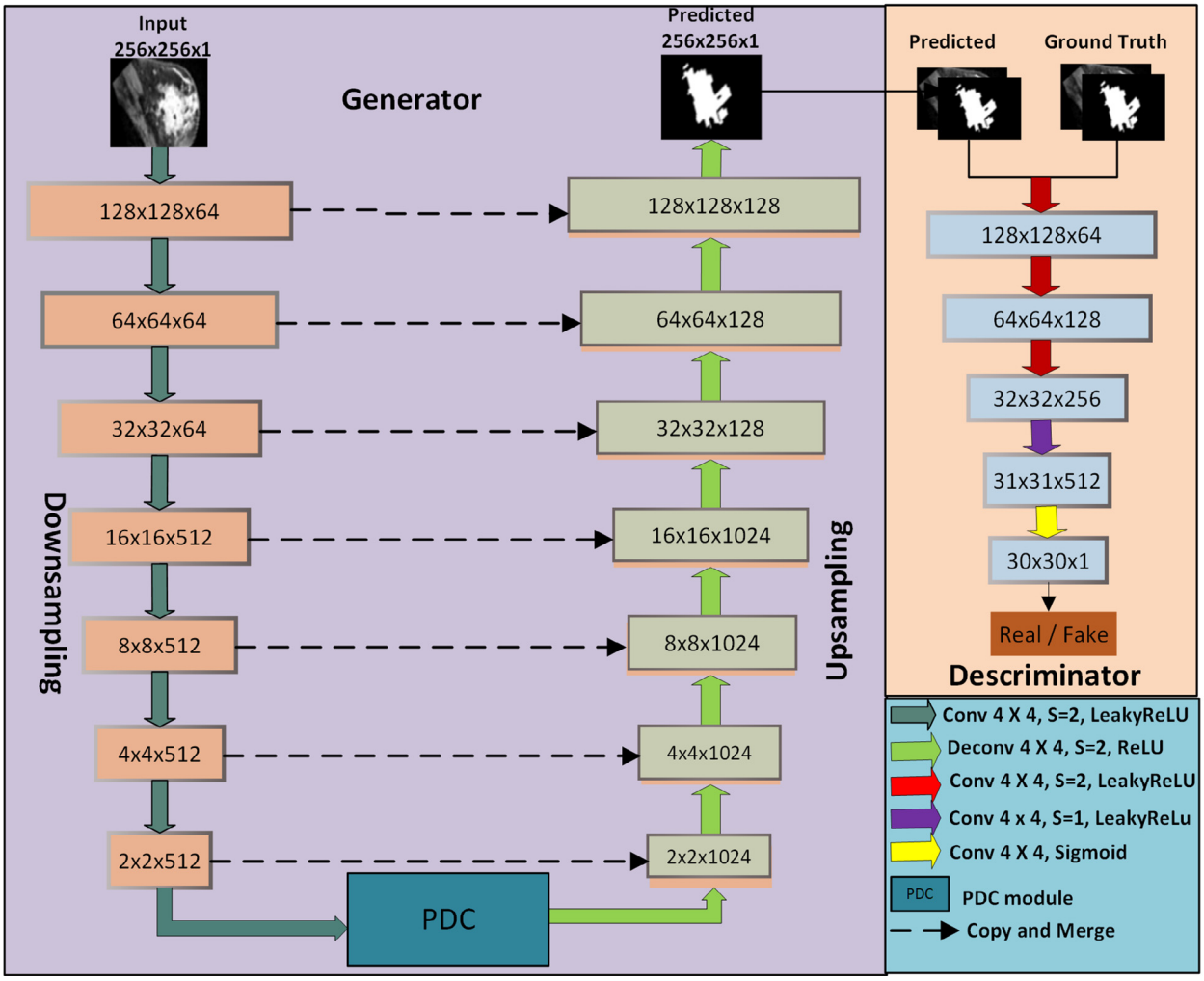

Fig. 4. Suggested BTS-GAN framework: generator G (left side), and discriminator D (right side).

mance of our approach. The dataset is accessible at The Cancer Imaging Archive (TCIA). The dataset comprises of DCE-MRI scans of different patients with ground truth segmentation. The ground truth segmentation part has been marked manually by the domain experts. Each scan is 288 x 288 in dimensions. The dataset is available in DICOM format having 60 slices per scan. Fig. 5 presents three samples from the RIDER MRI breast tumor dataset in the first row with their masks in the second row. A total of 500 breast MRI scans with ground truth masks were used for the experiment, divided in the ratio of 80:20 for training (400) and testing (100), respectively. As the number of datasets was relatively small, five-fold cross-validation was adopted in the experiment on this dataset. The training split was augmented (by randomly flipping horizontally and vertically, rotation, varying scale, gamma correction), to increase the dataset size to 3200. The dataset has been preprocessed and reshaped into 256 x 256 in dimensions.

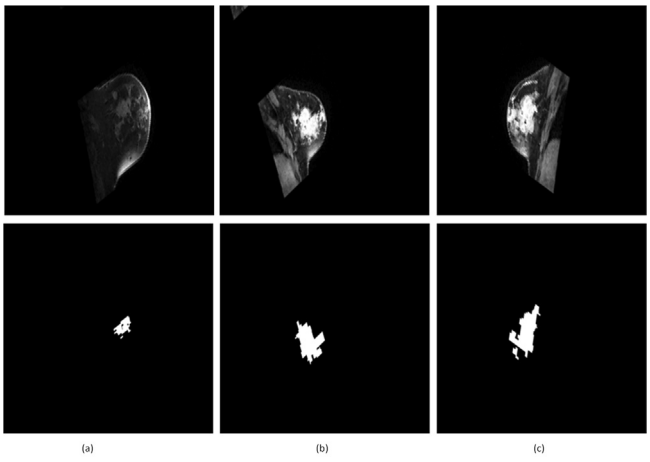

Fig. 5. RIDER breast MRI tumor images(1st row) in gray scale with their corresponding binary masks(2nd row).

3.2. Evaluation Metrics

To determine the model performance, the following standard measures were utilized to assess the image segmentation performance. We used the most common evaluation methods, i.e., IoU, dice similarity coefficient (DSC), True Positive Rate (TPR) and Misclassification Rate (MCR). These metrics, which range from 0 to 1, measure the performance of region-based segmentation from a variety of perspectives. The core values required to calculate these metrics are True Negatives (TN), False Negatives (FN), True Positives (TP), and False Positives (FP).

The overlap between the two samples is measured by the Dice. It's the most used measurement for grading segmentation tasks. It

computes the resemblance between the ground truth the generated segmentation masks. The higher the DSC, the more similar the generated result is to the ground truth. Let suppose I_p is our generated segmented image and I_t represent our ground truth image segmented by expert domain. Then DSC index can be written mathematically as:

$$\text{Dice}(I_p, I_t) = 2\frac{|I_p \cap I_t|}{|I_p| + |I_t|} \tag{7}$$

IoU is the ratio of the ground truth's intersection and union to the generated segmented image. The higher the IoU, the more accurate the segmentation. The IoU can be written mathematically as:

$$\text{Jaccard} = \text{IoU}(I_p, I_t) = \frac{|I_p \cap I_t|}{|I_p \cup I_t|} \tag{8}$$

Our predicted segmentation image and ground truth value are bound in between [0, 1]. Both of these measurement output value of 1 if there exists an overlapping between the I_p predicted mask and I_t ground truth and 0 in case of no overlapping. We can also write it in the confusion matrix form.

$$\text{Dice} = \frac{2\text{TP}}{(2\text{TP} + \text{FP} + \text{FN})} \tag{9}$$

$$\text{Jaccard} = \text{IoU} = \frac{\text{TP}}{(\text{TP} + \text{FP} + \text{FN})} \tag{10}$$

Other standard evaluation measures are also used to measure the segmentation error such as:

$$\text{TPF(Sensitivity)} = \frac{(I_p \cap I_t)}{I_t} \tag{11}$$

$$\text{MCR} = \frac{1 - (I_p \cap I_t)}{I_t} = 1 - \frac{\text{TP}}{(\text{TP} + \text{FN})} \tag{12}$$

Eq.(11) represents TPF also called Sensitivity. TPF is the fraction of true positives that are detected as such. A least 50% intersection between the generated output and ground truth was used to calculate the TPF. Eq.(12) shows the Misclassification Rate (MCR), which is previously applied to the brain segmentation problem [50]. The lower the value of MCR the better the model perform.

3.3. Model training

We used the standard technique from [33] to optimize our networks, such that one gradient descent step on D is preceded by one step on G. Rather of training G to minimize $log(1 - D(u, G(u, w)))$, as proposed in the original GAN study, we conversely train it to increase $logD(u, v)$. To choose the most optimal parameters of the network, hyperparameter tuning is applied. Table 1 shows the ranges used for hyperparameter tuning of the model. We used a λ value of 100 in Eq. 6, which shows the best results. We used Adam optimizer with a learning rate of 2×10^{-4}, momentum parameters β_1 = 0.50, β_2 = 0.99, and a batch vale of 24. Our BTS-GAN's optimization takes about 200 epochs to attain convergence. Results obtained from our proposed model were satisfactory and were evaluated using different standard metrics used in literature. We performed qualitative as well as quantitative analysis to validate our results. Our code is written in Python utilizing TensorFlow libraries and evaluated on a computer equipped with a NVIDIA GeForce GTX 1080 Ti GPU. The input images were resized to 256×256 pixels.

Table 1
Range for hyper parameter tuning applied.

Hyper Parameters	Range
Number of epochs	[100,150, 200, 250]
Lambda λ	[10 to 120]
Filter Size	[3,4,5,7]
Batch size	[16,24,32]
Dropout	[0.01,0.02,0.03,0.04]
Learning rate	$[2 \times 10^{-6}$ to $2 \times 10^{-3}]$

3.4. Ablation study

3.4.1. Impact of different loss functions

GAN and its variations, despite of its advantages, also have some disadvantages, one of which is the difficulty in converging. To overcome this problem in the I2I translation task, some methods chose to frame it as a regression task and thus added L1 and L2 separation as restrictions to the loss function of cGAN [43,51]. When a local minimum is attained during GAN's optimization procedure, these techniques give rough guidance for the system to proceed with gradient descent. However, this guidance works in limited situations, such as image colorization, where the target image is anticipated to consist of real-value pixels, nonetheless doesn't work for classification related problems, where the target image consists of discrete-value pixels, carrying class info. Therefore, we suggested that an extra classification connected loss L_{CE} is beneficial for this SS task.

To examine the effect of different losses, we trained our generator and BTS-GAN using the following combination of loss functions and recorded the DSC and IoU achieved in each case in Table 2. The first row shows the results when only the generator network was used for segmentation. As can be seen in the 2rd row, the DSC and IoU score drops significantly, when L_{CE} was removed from the objective loss function. It indicates that the GAN was experiencing the hard-to-converge problem when a classification-based task was formulated as a regression-based task.The 3rd row shows the outcomes when L_{CE} was used in combination with L_{cGAN}. The contributions provided by L_{L1} can also be seen in Table 2, by comparing 3rd and 4th rows, so we opted to use combination of all three.

3.4.2. Impact of PDC module

Table 3 shows the positive impact of the PDC module on the proposed model. The first row is the baseline U-Net, the second row is U-Net with PDC module, the third row is the BTS-GAN with the proposed loss function without PDC module, the last row shows the results of the proposed model with PDC module and full loss function in terms of DC, IoU, TPR, and MCR. The DSC of BTS-GAN is 10% and 5% higher than U-Net and improved U-Net, respectively. Similarly, the IoU, sensitivity, and MCR of BTS-GAN are also higher than U-Net and improved U-Net.

3.5. Quantitative Comparison

In this section we compare the segmentation results of our proposed model with the prior research work. Six distinct segmenta-

Table 2
Segmentation results using various loss functions for training.

Different combinations of loss functions	DSC	IoU
Generator only	0.804	0.723
BTS-GAN with L_{CE} removed	0.599	0.567
BTS-GAN with L_{L1} removed	0.845	0.768
BTS-GAN with L_{L1} + L_{CE} + L_{cGAN}	0.854	0.774

Table 3
The segmentation performance measures results using the three different DCNN models on test images from fivefold cross-validations.

Model	PDC	DSC	IoU	TPR	MCR
U-Net	No	0.752	0.675	0.792	0.208
Improved U-Net	Yes	0.804	0.725	0.842	0.158
BTS-GAN	No	0.807	0.747	0.872	0.128
BTS-GAN	Yes	0.854	0.774	0.934	0.076

tion techniques are selected specifically for this purpose. Five out of six were mentioned in the research by Bouchebbah et al.[52], namely Improved Self-Training (IMPST), Fuzzy C-Means (FCM), Bayesian, K-Nearest Neighbor (KNN), and Levels Propagation Approach (LPA). The other two studies are FCM and ALPA suggested by Chen et al.[53] and Bouchebbah et al. [54], respectively. The decision to use these approaches stems from the fact that they were all evaluated on the same RIDER MRI dataset and assessed using some or all of the assessment metrics described in "Evaluation Metrics". The experimental findings revealed that BTS-GAN has produced comparable segmentation outputs to other standard techniques and is able to be effectively used for BTS in MRI scans. The results obtained from the previous work and results from our proposed method are depicted in Table 4. For the BTS-GAN model, we obtained an average DSC of 0.85, 0.91 for the best case, and 0.77 was achieved in the worst case. The average DSC score of BTS-GAN is higher than both ALPA and FCM. The TPF maximum score is 0.97 with a mean value of 0.93, which is the highest TPF mean score of all the approaches. The IoU maximum, minimum, and average scores were 0.82,0.69, and 0.77, respectively. In addition, BTS-GAN's IoU mean score of 0.77 is higher than the best IoU mean of the other techniques. BTS-GAN also has a lower MCR mean of 0.07. As can be observed from Table 4 that the efficiency of the suggested segmentation model has outperformed other techniques. The improvement made by the proposed model is all due to our modification to the original U-NET and cGAN. The results clearly show that adding PDC module to the baseline U-Net model, using cGAN with a modified loss function, using BN, and the dropout at the first 3 layers of the decoder have the ability to improve the results of tumor segmentation.

3.6. Qualitative Comparison

For qualitative comparison, we selected three DL techniques, including the baseline U-Net, the modified U-Net (generator of BTS-GAN), and the proposed BTS-GAN model for BT segmentation. First, we compare the original and modified U-Net models to demonstrate the advantages of improving the network's feature retrieval capability. Second, in order to demonstrate the advantages of adversarial training, the suggested model was evaluated against modified U-Net.

Comparative segmentation results of both modified and original U-Nets can be seen in Fig. 6. In all the three cases shown, the basic U-Net gave FP segmentation and was not able to detect the edges of the tumor, but the modified U-Net segmented them significantly well. Despite the fact that the modified U-Net did not correctly segment the specifics of tumor edges, it performed much better than the baseline U-Net. The differences in segmentation between our BTS-GAN and the modified U-Net is shown in Fig. 7. The modified U-Net and BTS-GAN produced similar outputs in majority of samples from the test data. However, the modified U-Net segmentation outputs were still inconsistent, missing certain minor edges of the breast tumor in some cases, which were successfully detected by our BTS-GAN model. Both the generated binary mask and the ground truth mask have been presented in Fig. 7, which shows that our proposed model generates a binary mask similar in appearance to the ground truth.

Fig. 8 shows the box plot comparison of our proposed method versus our improved U-Net and baseline U-Net. The line inside each box indicates the median value; box limits include the interquartile ranges Q1 and Q3; upper and lower whiskers are cal-

Table 4
Quantitative comparison of BTS-GAN versus other approaches on RIDER dataset.

Methods	Metrics				
	Statistics	Dice	IoU	TPF	MCR
MASRG [55]	Max	–	–	0.99	0.48
	Mean	–	–	0.82	0.18
	Min	–	–	0.52	0.01
IMPST [56]	Max	–	–	0.96	0.62
	Mean	–	–	0.79	0.21
	Min	–	–	0.38	0.04
KNN [57]	Max	–	–	0.87	0.58
	Mean	–	–	0.73	0.27
	Min	–	–	0.42	0.13
Bayesian [58]	Max	–	–	0.95	0.70
	Mean	–	–	0.76	0.24
	Min	–	–	0.30	0.05
LPA [52]	Max	–	–	0.97	0.85
	Mean	–	–	0.90	0.11
	Min	–	–	0.77	0.02
FCM [53]	Max	0.77	0.71	0.80	0.35
	Mean	0.70	0.65	0.72	0.28
	Min	0.63	0.60	0.65	0.20
ALPA [54]	Max	0.81	0.75	0.91	0.37
	Mean	0.74	0.67	0.74	0.26
	Min	0.65	0.60	0.63	0.09
BTS-GAN	Max	0.91	0.82	0.97	0.16
	Mean	**0.85**	**0.77**	**0.93**	**0.07**
	Min	0.77	0.69	0.78	0.03

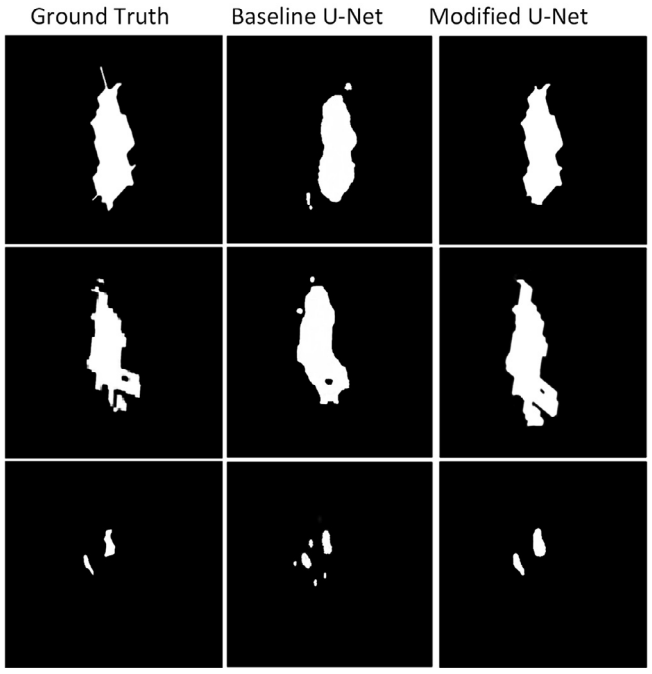

Fig. 6. Comparative results of baseline and modified U-Net on three MRI scans (results are zoomed out for clear demonstration).

culated as 1.5 times the distance between the upper and lower box limits; and all values outside the whiskers are assumed outliers, which are indicated by circles. DSC and IoU values were plotted using 100 testing samples of the dataset. Our cGAN-based model had a narrow range of DSC and IoU values, whereas U-Net showed a wider range of values. There are numerous outliers in the segmentation results of the state-of-the-art U-Net method, whereas the proposed method generated no outliers. We also calculated the inference time of the above three models. U-Net, improved U-Net, and the proposed BTS-GAN achieved 21.13, 22.26, and 19.84 frames per second, respectively.

4. Discussion

This research uses the cGAN model to suggest an automated DL approach for segmenting breast cancer tumors utilizing DCE-MRI scans. We examined the limitations of the basic U-Net architecture in BTS and came up with a two-step solution. Firstly, we modified the U-Net to improve the model's potential to extract features by adding skip connections and PDC module between encoder and decoder. Then, we introduced adversarial training with a modified loss function to improve the segmentation result's stability and accuracy. We establish a classification-related limit for optimizing cGAN, which helps to reduce the convergence problem for the breast lesions segmentation. The model was evaluated with and without using the CE loss term in the objective function of BTS-GAN and proved that our proposed loss function got best accuracy. The proposed method has been trained and evaluated using standard segmentation performance measures. We discovered that extending the number of training examples significantly enhanced training outcomes by employing standard augmentation methods, but adding more augmented training samples did not improve the outcomes. After training, the model provides satisfactory results on our testing data.

The results from the suggested model and previous standard techniques have been depicted, which shows that the outcomes of the suggested model are quite satisfactory on the RIDER dataset compared to other approaches. We achieved an average DSC score of 0.85, IoU of 0.77, 0.93 for TPF, and 0.07 for MCR confirming that BTS-GAN performed better than other approaches.

Although our model performed well on most MRI scans and got better segmentation results in challenging cases, it still gave some individual unsatisfactory results, shown in Fig. 9. As can be seen in the first row, in this particular MRI scan, it is even difficult for a naked eye to decide whether the area under the red box is a tumor or not, which our model detected as a tumor. In the 2nd row, our model detected the tumor inside the green box but could not detect the sharp edges. Figs. 6, 7, and 9, are zoomed out for demonstration purposes.

Several deeper designs were explored in our study, but no significant improvement was observed. Furthermore, training deeper designs is more challenging, particularly for adversarial networks. Using pooling layers in BTS-GAN did not enhance our results either. As a result, following the approach of DCGAN [59], we used convolution layers with the stride of 2 to achieve feature downsampling. The model performed well with batch normalization compare to instance normalization, which does not learn the area with a small number of binary mask pixels. The proposed model can be used for other imaging modalities, like mammograms and BUS scans, to perform binary tumor segmentation by training model with respective imaging modalities. In the future, our goal is to experiment with other imaging modalities, convert the model to multi modalities segmentation model and make it more robust.

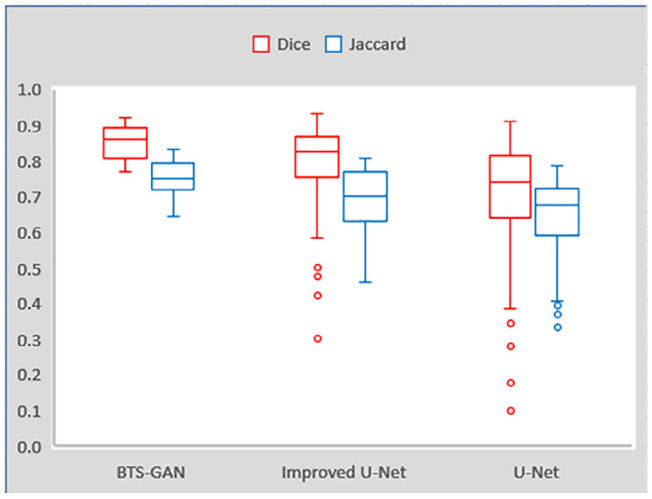

Fig. 8. Boxplots of DSC and IoU scores for all test samples.

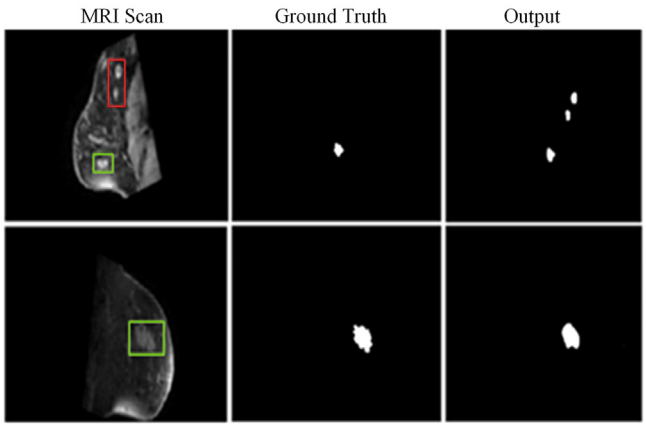

Fig. 9. Cases of poor mass segmentation results.

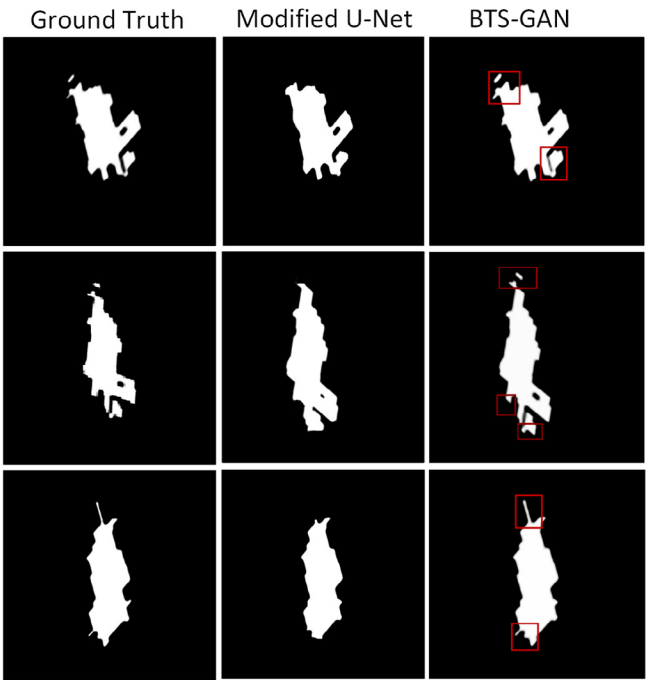

Fig. 7. Comparative results of the modified U-Net and the BTS-GAN on three MRI scans (results are zoomed out for clear demonstration).

5. Conclusion

Automatic and precise tumor segmentation from breast MRI scans is the subject of this article. We offer a cGAN based solution (BTS-GAN) to this challenge to create tumor masks near the ground truth masks by adding a PDC module in our generator network and using a modified objective function for our model. We conducted different experiments with our BTS-GAN and presented the qualitative and quantitative measures. Overall the network performed very well and got an average DSC score of 85% and IoU of 77%, outperforming other methods. In future, our goal is to experiment the model with other imaging modalities, convert the model to multi modalities segmentation model, and make it robust.

Data Availability

In our experiments, the Reference Image Database to Evaluate Therapy Response (RIDER) breast MRI data-set was used to assess the efficiency of the suggested approach. The data is publicly available at The Cancer Imaging Archive (TCIA).

Declaration of Competing Interest

The authors declare that they have no known competing financial interests or personal relationships that could have appeared to influence the work reported in this paper.

Acknowledgement

This work is supported by the National Natural Science Foundation of China (NSFC Grant No. 62073260).

References

[1] F. Bray, J. Ferlay, I. Soerjomataram, R.L. Siegel, L.A. Torre, A. Jemal, Global cancer statistics 2018: Globocan estimates of incidence and mortality worldwide for 36 cancers in 185 countries, CA: A Cancer Journal for Clinicians 68 (6) (2018) 394–424.
[2] M. Amin, American cancer society, AJCC cancer staging manual, Eight edition/ editor-in-chief, Mahul B. Amin, MD, FCAP..
[3] M. Liu, S.X. Tang, J.Y. Tsang, Y.J. Shi, Y.B. Ni, B.K. Law, M. Gary, Core needle biopsy as an alternative to whole section in ihc4 score assessment for breast cancer prognostication, Journal of clinical pathology 71 (12) (2018) 1084–1089.
[4] Q. Huang, Y. Luo, Q. Zhang, Breast ultrasound image segmentation: a survey, International journal of computer assisted radiology and surgery 12 (3) (2017) 493–507.
[5] J. Zhang, B. Chen, M. Zhou, H. Lan, F. Gao, Photoacoustic image classification and segmentation of breast cancer: A feasibility study, IEEE Access 7 (2018) 5457–5466.
[6] A. Saha, X. Yu, D. Sahoo, M.A. Mazurowski, Effects of mri scanner parameters on breast cancer radiomics, Expert systems with applications 87 (2017) 384–391.
[7] C. Militello, L. Rundo, M. Dimarco, A. Orlando, V. Conti, R. Woitek, I. D'Angelo, T. V. Bartolotta, G. Russo, Semi-automated and interactive segmentation of contrast-enhancing masses on breast dce-mri using spatial fuzzy clustering, Biomedical Signal Processing and Control 71 (2022) 103113.
[8] R. Malladi, J.A. Sethian, B.C. Vemuri, Shape modeling with front propagation: A level set approach, IEEE transactions on pattern analysis and machine intelligence 17 (2) (1995) 158–175.
[9] S. Beucher, Use of watersheds in contour detection, in: Proceedings of the International Workshop on Image Processing, CCETT..
[10] R. Adams, L. Bischof, Seeded region growing, IEEE Transactions on pattern analysis and machine intelligence 16 (6) (1994) 641–647.
[11] B. Manjunath, R. Chellappa, Unsupervised texture segmentation using markov random field models, IEEE transactions on pattern analysis and machine intelligence 13 (5) (1991) 478–482.
[12] M. Kass, A. Witkin, D. Terzopoulos, Snakes: Active contour models, International journal of computer vision 1 (4) (1988) 321–331.
[13] A.A. Nahid, Y. Kong, Histopathological breast-image classification using local and frequency domains by convolutional neural network, Information 9 (1) (2018) 19.
[14] A.A. Nahid, M.A. Mehrabi, Y. Kong, Histopathological breast cancer image classification by deep neural network techniques guided by local clustering, BioMed research international (2018).
[15] H. Ali, H. Li, E. Afele Retta, I.U. Haq, Z. Guo, X. Han, L. Cui, L. Yang, J. Feng, Representation of differential learning method for mitosis detection, Journal of Healthcare, Engineering (2021).
[16] V. Badrinarayanan, A. Kendall, R. Cipolla, Segnet: A deep convolutional encoder-decoder architecture for image segmentation, IEEE transactions on pattern analysis and machine intelligence 39 (12) (2017) 2481–2495.
[17] C. Zhang, Y. Song, S. Liu, S. Lill, C. Wang, Z. Tang, Y. You, Y. Gao, A. Klistorner, M. Barnett, Ms-gan: Gan-based semantic segmentation of multiple sclerosis lesions in brain magnetic resonance imaging, in: 2018 Digital Image Computing: Techniques and Applications (DICTA), IEEE, pp. 1–8..
[18] Y. Huo, Z. Xu, H. Moon, S. Bao, A. Assad, T.K. Moyo, M.R. Savona, R.G. Abramson, B.A. Landman, Synseg-net: Synthetic segmentation without target modality ground truth, IEEE transactions on medical imaging 38 (4) (2018) 1016–1025.
[19] G. Piantadosi, M. Sansone, R. Fusco, C. Sansone, Multi-planar 3d breast segmentation in mri via deep convolutional neural networks, Artificial Intelligence in Medicine 103 (2020) 101781.
[20] H. Wang, J. Cao, J. Feng, Y. Xie, D. Yang, B. Chen, Mixed 2d and 3d convolutional network with multi-scale context for lesion segmentation in breast dce-mri, Biomedical Signal Processing and Control 68 (2021) 102607.
[21] P. Yousefikamal, Breast tumor classification and segmentation using convolutional neural networks, arXiv preprint arXiv:1905.04247..
[22] R. Almajalid, J. Shan, Y. Du, M. Zhang, Development of a deep-learning-based method for breast ultrasound image segmentation, in: 2018 17th IEEE International Conference on Machine Learning and Applications (ICMLA), IEEE, pp. 1103–1108..
[23] J. Long, E. Shelhamer, T. Darrell, Fully convolutional networks for semantic segmentation, in: Proceedings of the IEEE conference on computer vision and pattern recognition, pp. 3431–3440..
[24] O. Ronneberger, P. Fischer, T. Brox, U-net: Convolutional networks for biomedical image segmentation, in: International Conference on Medical image computing and computer-assisted intervention, Springer, pp. 234–241..
[25] P. Moeskops, J.M. Wolterink, B.H. van der Velden, K.G. Gilhuijs, T. Leiner, M.A. Viergever, I. I'gum, Deep learning for multi-task medical image segmentation in multiple modalities, in: International Conference on Medical Image Computing and Computer-Assisted Intervention, Springer, pp. 478–486..
[26] M.A. Al-Antari, M.A. Al-Masni, M.T. Choi, S.M. Han, T.S. Kim, A fully integrated computer-aided diagnosis system for digital x-ray mammograms via deep learning detection, segmentation, and classification, International journal of medical informatics 117 (2018) 44–54.
[27] G. Tong, Y. Li, H. Chen, Q. Zhang, H. Jiang, Improved u-net network for pulmonary nodules segmentation, Optik 174 (2018) 460–469.
[28] S. Ioffe, C. Szegedy, Batch normalization Accelerating deep network training by reducing internal covariate shift, in: International conference on machine learning, PMLR, 2015, pp. 448–456.
[29] Z. Zhuang, A.N.J. Raj, A. Jain, N. Ruban, S. Chaurasia, N. Li, M. Lakshmanan, M. Murugappan, Nipple segmentation and localization using modified u-net on breast ultrasound images, Journal of Medical Imaging and Health Informatics 9 (9) (2019) 1827–1837.

[30] Z. Zhuang, N. Li, A.N. Joseph Raj, V.G. Mahesh, S. Qiu, An rdau-net model for lesion segmentation in breast ultrasound images, PloS one 14 (8) (2019) e0221535.
[31] H. Jiao, X. Jiang, Z. Pang, X. Lin, Y. Huang, L. Li, Deep convolutional neural networks-based automatic breast segmentation and mass detection in dce-mri, Computational and Mathematical Methods in Medicine (2020).
[32] M.U. Dalmis, G. Litjens, K. Holland, A. Setio, R. Mann, N. Karssemeijer, A. Gubern-Mérida, Using deep learning to segment breast and fibroglandular tissue in mri volumes, Medical physics 44 (2) (2017) 533–546.
[33] I. Goodfellow, J. Pouget-Abadie, M. Mirza, B. Xu, D. Warde-Farley, S. Ozair, A. Courville, Y. Bengio, Generative adversarial nets, in: Advances in neural information processing systems, pp. 2672–2680..
[34] W.C. Hung, Y.H. Tsai, Y.T. Liou, Y.Y. Lin, M.H. Yang, Adversarial learning for semi-supervised semantic segmentation, arXiv preprint arXiv:1802.07934..
[35] Z. Shi, Q. Hu, Y. Yue, Z. Wang, O.M.S. AL-Othmani, H. Li, Automatic nodule segmentation method for ct images using aggregation-u-net generative adversarial networks, Sensing and Imaging 21 (1) (2020) 1–16.
[36] S. Kohl, D. Bonekamp, H.P. Schlemmer, K. Yaqubi, M. Hohenfellner, B. Hadaschik, J.P. Radtke, K. Maier-Hein, Adversarial networks for the detection of aggressive prostate cancer, arXiv preprint arXiv:1702.08014..
[37] F. Gao, T. Wu, X. Chu, H. Yoon, Y. Xu, B. Patel, Deep residual inception encoder-decoder network for medical imaging synthesis, IEEE journal of biomedical and health informatics 24 (1) (2019) 39–49.
[38] Y. Xue, T. Xu, H. Zhang, L.R. Long, X. Huang, Segan: Adversarial network with multi-scale l 1 loss for medical image segmentation, Neuroinformatics 16 (3) (2018) 383–392.
[39] X. Ma, J. Wang, X. Zheng, Z. Liu, W. Long, Y. Zhang, J. Wei, Y. Lu, Automated fibroglandular tissue segmentation in breast mri using generative adversarial networks, Physics in Medicine & Biology 65 (10) (2020) 105006.
[40] A. Negi, A.N.J. Raj, R. Nersisson, Z. Zhuang, M. Murugappan, Rda-unet-wgan: an accurate breast ultrasound lesion segmentation using wasserstein generative adversarial networks, Arabian Journal for Science and Engineering 45 (8) (2020) 6399–6410.
[41] K. Armanious, C. Jiang, M. Fischer, T. Kstner, T. Hepp, K. Nikolaou, S. Gatidis, B. Yang, Medgan: Medical image translation using gans, Computerized medical imaging and graphics 79 (2020) 101684.
[42] V.K. Singh, H.A. Rashwan, S. Romani, F. Akram, N. Pandey, M.M.K. Sarker, A. Saleh, M. Arenas, M. Arquez, D. Puig, Breast tumor segmentation and shape classification in mammograms using generative adversarial and convolutional neural network, Expert Systems with Applications 139 (2020) 112855.
[43] P. Isola, J.Y. Zhu, T. Zhou, A.A. Efros, Image-to-image translation with conditional adversarial networks, in: Proceedings of the IEEE conference on computer vision and pattern recognition, pp. 1125–1134..
[44] M. Cordts, M. Omran, S. Ramos, T. Rehfeld, M. Enzweiler, R. Benenson, U. Franke, S. Roth, B. Schiele, The cityscapes dataset for semantic urban scene understanding, in: Proceedings of the IEEE conference on computer vision and pattern recognition, pp. 3213–3223..
[45] P.Y. Laffont, Z. Ren, X. Tao, C. Qian, J. Hays, Transient attributes for high-level understanding and editing of outdoor scenes, ACM Transactions on graphics (TOG) 33 (4) (2014) 1–11.
[46] S. Hwang, J. Park, N. Kim, Y. Choi, I. So Kweon, Multispectral pedestrian detection: Benchmark dataset and baseline, in: Proceedings of the IEEE conference on computer vision and pattern recognition, pp. 1037–1045..
[47] N. Bayramoglu, M. Kaakinen, L. Eklund, J. Heikkila, Towards virtual h&e staining of hyperspectral lung histology images using conditional generative adversarial networks, in: Proceedings of the IEEE International Conference on Computer Vision Workshops, 2017, pp. 64–71.
[48] P. Wang, P. Chen, Y. Yuan, D. Liu, Z. Huang, X. Hou, G. Cottrell, Understanding convolution for semantic segmentation, in: 2018 IEEE winter conference on applications of computer vision (WACV), Ieee, 2018, pp. 1451–1460.
[49] F. Yu, V. Koltun, Multi-scale context aggregation by dilated convolutions, arXiv preprint arXiv:1511.07122..
[50] T. Song, C. Gasparovic, N. Andreasen, J. Bockholt, M. Jamshidi, R.R. Lee, M. Huang, A hybrid tissue segmentation approach for brain mr images, Medical and Biological Engineering and Computing 44 (3) (2006) 242–249.
[51] J.D.T.D.A.A.E.D. Pathak, P. Krahenbuhl, Context encoders: Feature learning by inpainting, in: Proceedings of the IEEE conference on computer vision and pattern recognition, pp. 2536–2544..
[52] F. Bouchebbah, H. Slimani, Levels propagation approach to image segmentation: Application to breast mr images, Journal of digital imaging 32 (3) (2019) 433–449.
[53] D.R. Chen, Y.W. Chang, H.K. Wu, W.C. Shia, Y.L. Huang, Multiview contouring for breast tumor on magnetic resonance imaging, Journal of digital imaging 32 (5) (2019) 713–727.
[54] F. Bouchebbah, H. Slimani, 3d automatic levels propagation approach to breast mri tumor segmentation, Expert Systems with Applications 165 (2021) 113965.
[55] A.Q. Al-Faris, U.K. Ngah, N.A.M. Isa, I.L. Shuaib, Computer-aided segmentation system for breast mri tumour using modified automatic seeded region growing (bmri-masrg), Journal of digital imaging 27 (1) (2014) 133–144.
[56] R. Azmi, N. Norozi, R. Anbiaee, L. Salehi, A. Amirzadi, Impst: a new interactive self-training approach to segmentation suspicious lesions in breast mri, Journal of medical signals and sensors 1 (2) (2011) 138.
[57] E. Fix, J. Hodges, Discriminatory analysis: nonparametric discrimination: consistency properties. report. 4, T. USAF School of Aviation Medicine..
[58] Q. Wu, M. Salganicoff, A. Krishnan, D.S. Fussell, M.K. Markey, Interactive lesion segmentation on dynamic contrast enhanced breast mri using a markov model, in: Medical Imaging 2006: Image Processing, vol. 6144, International Society for Optics and Photonics, p. 61444M..
[59] A. Radford, L. Metz, S. Chintala, Unsupervised representation learning with deep convolutional generative adversarial networks, arXiv preprint arXiv:1511.06434..